

Real-time comprehensive control over soliton molecules

Lilin Yi (✉ lilinyi@sjtu.edu.cn)

Shanghai Jiao Tong University

Chao Luo

Shanghai Jiao Tong University

Guoqing Pu

Shanghai Jiao Tong University

Zhiwei Fang

Shanghai Jiao Tong University

Yong Wu

Shanghai Jiao Tong University

Jiajin Wang

Shanghai Jiao Tong University

Weisheng Hu

Shanghai Jiao Tong University

Article

Keywords:

Posted Date: August 29th, 2023

DOI: <https://doi.org/10.21203/rs.3.rs-3258413/v1>

License:  This work is licensed under a Creative Commons Attribution 4.0 International License.

[Read Full License](#)

Abstract

Soliton molecules, the bound aggregation of sub-solitons, inherently own multi-dimensional properties, thereby manifesting substantial potential in optical communications and optical data storage. However, to release the potential demands the control ability over multi-dimensions of soliton molecules, by which the valid information can be modulated onto these dimensions. Here, we propose a real-time feedback scheme governed by a dedicated-designed two-step optimization algorithm for comprehensively controlling soliton molecular multi-dimensional properties. This technique can manipulate inter-soliton separations and relative intensities of soliton molecules in a basic nonlinear-polarization-evolution-based mode-locked fiber laser. The wide tuning range over the inter-soliton separation from 2 ps to 58 ps is achieved, and seamless tuning with a precision of 0.05 ps is demonstrated. Relative intensities between solitons can also be separately controlled and a two-dimensional joint regulation is performed. Moreover, the real-time transmission over 30-km single-mode fiber is demonstrated and spectral period doubling of soliton molecules is captured, further manifesting the validity of the comprehensive control method.

Introduction

Mode-locked fiber lasers (MLFLs), renowned for their superior output pulse attributes, serve tremendous applications such as biological imaging^{1,2}, frequency comb spectroscopy³, material fabrication^{4,5}, lidar^{6,7}, high-resolution atomic clocks^{8,9}, precision metrics¹⁰, and astronomy¹¹. As a special aggregation of soliton wave packets produced by MLFLs, soliton molecules (SMs) have attracted a lot of attention in the field of ultrafast laser dynamics since its emergence as a result of the simulation models based on the Schrödinger and Ginzburg-Landau equations^{12,13} and its first experimental observation¹⁴. SMs can be considered as a unique bound state tied by the equilibrium of attractive and repulsive forces between paired sub-pulses in each period¹⁵⁻¹⁹. For instance, the most common SM consists of two solitons with a fixed inter-soliton separation, whose spectrum is regularly modulated with a fringe period determined by the temporal inter-soliton separation²⁰. Passive MLFLs with abundant intra-cavity nonlinear dynamics have proven to be prolific sources of SMs²¹, spawning an array of soliton molecular varieties ranging from stable or oscillatory SMs^{14,22-24} with varying phase stability to loosely or tightly bound SMs^{22,25} with different separations. The implementation of time-stretch dispersion Fourier transform (TS-DFT) techniques²⁶, a spectral-to-temporal mapping method enabling real-time spectra acquisition, has further facilitated direct observation of inherent nonlinear evolutionary dynamics related to the generation and evolution of SMs²⁷⁻⁴¹. On the other hand, compared to conventional solitons, SMs provides new possibilities for optical communication⁴²⁻⁴⁸, storage⁴⁹⁻⁵¹ and all-optical switching⁵² due to their extra dimensions including inter-soliton separation, relative intensity and phase. Therefore, it is imperative to realize control over diverse dimensions of SMs.

Recently, partial control over SMs has been demonstrated via altering laser parameters containing cavity length, pump power, and intra-cavity dispersion^{25,50,51,53,54}. The inclusion of a unique composite fiber inside the cavity acting as a saturable absorber facilitates the transition between loosely and tightly

bound SMs via mechanical adjustment²⁵. Pump power control manifests itself as a reliable method of controlling SMs through both experimental observations and the analysis of fundamental principles⁵³. Four types of SMs distinguished by relative phase are generated by direct pump-current control⁵⁰. An alternative control strategy involves the manipulation of group-velocity dispersion and dispersion losses at specific wavelength positions via incorporating spatial light modulation (SLM) based on a 4-f system in the cavity, enabling direct control over SMs generation with inter-soliton separations ranging from 3 ps to nearly 13 ps⁵¹. Another study also incorporating the intra-cavity 4-f system enabled SLM and an offline close-loop scheme can produce SMs with tunable inter-soliton separations from 3 ps to 8 ps⁵⁴.

Previous studies mainly concentrate on merely one dimension of SMs while omitting the control over rest properties of SMs. Second, the introduction of SLM substantially enhances the system complexity hindering the potential wide utilizations of the programmable SM light source. More importantly, the precision of open-loop direct control^{25,50,51,53} subjects to the stabilities of various components and environments, which cannot be guaranteed in many situations. The inherent and unpredictable hysteresis phenomenon of SMs²⁰ may further increase the control error when open-loop control is applied. The offline close-loop control can reduce the imperfections induced control error⁵⁴ but the searching phase can be rather time-consuming. As a result, comprehensive and precise manipulation on the properties (i.e., the inter-soliton separation, relative intensity and phase) of SMs in a real-time manner in order to meet application-specific requirements remains a public challenge to be conquered.

Here, we propose a real-time close-loop comprehensive control strategy over SMs in a simple and basic nonlinear-polarization-evolution (NPE) MLFL. Via combining TS-DFT and a high-speed analog-to-digital converter (ADC), single-shot spectrum acquisition with a frame rate of 43.1 MHz serves as the close-loop input. Sequential single-shot spectrum analysis and a dedicated-designed searching algorithm run on a field-programmable gate array (FPGA), and then the FPGA commands digital-to-analog converters (DACs) to alter pump power and the polarization with an electronic polarization controller (EPC). As a result, various SMs with different inter-soliton separations can be automatically searched. By encoding SMs with various inter-soliton separations as different binary bits, we successfully demonstrate real-time transmission using various SMs, where a string "SJTU" is encoded and then transmitted over 30-km single-mode fiber (SMF). Benefited from the real-time control, the spectral period doubling of SMs is experimentally captured for the first time. The offline close-loop scheme is also demonstrated, where a wide tuning range from 2 ps to 58 ps of the inter-soliton separation is achieved in virtue of a high-resolution optical spectrum analyzer (OSA) and the control precision even reaches 0.05 ps. Further, automatic control over another dimension, the relative intensity between two solitons, is experimentally exhibited through analyzing on the spectral modulation depth. With the comprehensive control over the inter-soliton separation and the relative intensity, special SMs with nearly identical inter-soliton separations but different relative intensities can be automatically located. The proposed comprehensive control over SMs in a basic NPE MLFL is the most compact solution in controlling SMs generation to date, thereby providing an ideal breeding ground for both diverse applications in optical signal transmission and optical storage and the research on SM-related laser dynamics.

Results

Experimental setups and principles. Figure 1a shows a custom-built, erbium-doped MLFL used to study the generation of SMs. The short cavity and high gain coefficient erbium-doped fiber (EDF) are employed to create conditions more conducive to SM production⁵⁵ (see Materials and Methods). The laser includes an isolator for unidirectional operation and a 20/80 coupler for signal output. A 980nm laser serves as the power source, with an initial power of 140 mW, coupled through a wavelength division multiplexer (WDM). The primary control element for intracavity polarization is the EPC, which has a microsecond-level response and is driven by four DACs. The EPC and the polarizer together form artificial saturable absorption, the fundamental mechanism in NPE-based mode-locking. In the offline close-loop control, the spectra acquired by an OSA are transmitted to a computer, which serves as the core for algorithm running. The computer sends commands to the FPGA based on the optimization algorithm results, setting DAC voltages to drive the four-phase retarders of the EPC and the pump power. However, in the real-time close-loop control, real-time spectra acquisition is achieved via TS-DFT. The algorithm runs directly on the FPGA and the sequential controlling part is identical to the offline scheme.

To achieve comprehensive control over SMs, the design of searching algorithm is vital. The core algorithm consists of two major steps as depicted in Fig. 1b. The first step is to locate the mode-locking states, which is governed by the modified genetic algorithm (GA), a GA with drop out based on the discrimination of mode-locking states⁵⁶. The full width at half maximum (FWHM) is used as the fitness to distinguish between the continuous wave state and mode-locking states. The second step is fine tuning after the mode-locking states are located. The two-step algorithmic design is due to the SMs are usually generated from the mode-locking states. Besides, the transformation among different SMs generally only requires a minor perturbation on polarization and pump power. Therefore, a fine-tuning stage is a suitable solution, where the pump and EPC are driven by well-designed perturbation signals. The fitness in the fine-tuning stage is either the inter-soliton separation or the side-to-peak ratio (SPR) of the SM (see Materials and Methods). The inter-soliton separation represents the temporal interval between the two solitons, determining the spectral modulation period based on the time-frequency correspondence²⁰. The SPR is the ratio of one side peak to the main peak on the autocorrelation trace, indicating the relative strength of the two solitons and determining the spectral modulation depth (see Materials and Methods). Note that the number of consecutive detachments (i.e., detached from mode-locking states) is recorded. If the number exceeds a preset threshold on the number of consecutive detachments, the algorithm will relaunch the modified GA for searching mode-locking states to avoid getting trapped in local areas corresponding to unlocked states. Finally, the search is completed when current fitness reaches the allowed range centered at the target fitness.

Comprehensive control over SMs. We first validate comprehensive control over SMs using the offline scheme and Fig. 2 shows the search results for SMs with various inter-soliton separations. The left panel in Fig. 2a depicts the searched spectra with separations spanning from 2 ps to 58 ps, where the SM with a separation of 11 ps has a larger central wavelength shift compared to others. As the separation increases, the spectral modulation becomes denser, which is consistent with the interference of two

solitons. The right part of Fig. 2a shows the calculated autocorrelation traces using the spectra. Only the right halves of the autocorrelation traces are shown since the calculated autocorrelations are symmetric. In this case, the error threshold on the inter-soliton separation is set as 0.5 ps, which is a relatively loose exit condition to avoid excessive time consumption. For more precise control, even smaller perturbations are applied to meet an error threshold on the inter-soliton separation of merely 0.05 ps. Figure 2b illustrates spectra and the corresponding autocorrelation traces of the high-precision control over the inter-soliton separation. 8 curves depict different SMs with inter-soliton separations ranging from 3 ps to 3.7 ps with an interval of 0.1 ps. Although the spectral differences are negligible, the autocorrelation traces reveal a distinct trend of increasing separation. The searching outcomes and error analysis are displayed at the top of Fig. 2c, which statistically compares the target separations with the searched separations. The blue dashed line represents the ideal curve, while the red dots represent the searched separations, which are very close to the target separations. The errors between the target separations and the searched separations are depicted at the bottom of Fig. 2c. The errors are all less than 0.05 ps in the precise tuning range, indicating excellent reliability of the searching algorithm.

The relative intensity between two solitons can also be automatically adjusted by using SPR as the fitness. Several SMs with SPRs ranging from 37–49% have been experimentally realized. Figure 3a, b show three sets of spectra and autocorrelation traces with different SPRs. It is obvious that the spectral modulation depth increases as SPR increases. The autocorrelation traces shown in Fig. 3b demonstrate that the inter-soliton separation varies from 5.3 ps to 30.2 ps with different SPRs, which is the result of the global search only focusing on SPR. To further investigate the capability of comprehensive control, the joint search combining both dimensions is performed. Concretely, the algorithm is required to search a pair of SMs, whose inter-soliton separations are nearly identical but SPRs are different. Figure 3c shows the joint search result. The searched two SMs have separations near 4 ps with a difference of only 0.08 ps, while the corresponding SPRs are 40% and 49%, respectively. Theoretically, given enough spectral resolution, the proposed scheme suits for joint search diverse SMs in multiple dimensions.

Soliton separation modulation (SSM)-based real-time transmission. To meet the increasing demand for information transmission, composite encoding in a single clock cycle is widely used^{42,50,51}. SMs inherently carrying multidimensional information in a single roundtrip provides new possibilities for advanced modulation formats. Here, via shifting the offline control to the real-time control with algorithms entirely integrated into the FPGA, we demonstrate real-time synchronized transmission over 30-km SMF utilizing the inter-soliton separations of SMs in Fig. 4. Compared to individual encoding, the stability requirement of encoding and decoding in transmission places higher demands on the accuracy and repeatability of the real-time control, thereby challenging the system logic and the capability of the optimization algorithm. The transmitter (Tx) is an MLFL with real-time comprehensive control over SMs. The 30-km SMF not only serves as the transmission medium, but also provides necessary dispersion for performing TS-DFT on the sent SMs. Otherwise, the picosecond-level separations cannot be discriminated by a 4-GSa/s ADC. The receiver (Rx) is implemented using another set of a PD, an ADC, and

an FPGA with the same parameters. Whole encoding, decoding, and search control processes are performed by two FPGAs without additional human intervention.

Five signals are used to realize transmission, including a start (i.e., “STA”) or end signal (i.e., “END”) for synchronizing between the Tx and the Rx, and four 2-bit binary combinations (i.e., “00”, “01”, “10”, “11”) carrying valid information. The five signals are encoded with five distinct inter-soliton separation regions, with some redundancies between them to increase system robustness against noise. We term the inter-soliton-separation-based encoding method as SSM and SSM-4 is applied here. Figure 5 illustrates a concise synchronized communication protocol and the mapping between signals and the inter-soliton separations. The Tx initiates a search for the start signal, whereas the Rx continually evaluates the current state. When the start signal appears, both the Tx and the Rx simultaneously enter the valid information transmission stage and initiate their respective internal timer. A sending period of 30 s is defined and guaranteed by a timer interrupt in both FPGAs to ensure accurate synchronization. In each sending period, the Tx searches the desired SM carrying the desired signal to send through the algorithm and maintains the state till the end of the sending period. On the other hand, the Rx obtains the average data of 3 acquisitions via the ADC after waiting for 28 s in each sending period. Then, the Rx decodes the received signal and waits till the sending period finishes. When all valid signals are transmitted, the Tx searches the end signal and maintains it in the final sending period. Once the Rx receives the end signal, both sides enter standby mode simultaneously and wait for the next transmission.

Sixteen consecutive 2-bit valid signals representing the ASCII of the string “SJTU” in binary form (i.e., “S”-“01010011”, “J”-“01001010”, “T”-“01010100”, “U”-“01010101”) are used to demonstrate the transmission. The left one in Fig. 6a shows the real-time spectra of search SMs on the Tx side, where each SM shows for 10 roundtrips. There are 180 roundtrips in total including the start and end signals. Obviously, different signals correspond to different spectral patterns. The right one in Fig. 6a presents the statistics of inter-soliton separations calculated from real-time spectra, with five signals highlighted in five colors. Inter-soliton separations of five signals are clearly distinguishable. Small separation variation in the same signal originates from ADC sampling error due to the limited sampling rate and the effective number of bits. Note that intermittent roundtrips in the start or end signal below 3.5 ps do not influence the transmission since the mean separation over 10 roundtrips is used for decision. The pink line (at the right of Fig. 6a) depicts the time spent by the Tx side searching valid signals, with nearly half of the time consumption below 1 s and the average time consumption of 3.84 s. The longest search costs 23.9 s, probably due to the rather small solution space and environmental disturbances. The single-loop time of perturbation in the algorithm is 0.2 s, including real-time spectra acquisition, algorithm processing, and a delay of 0.1 s for the SM stabilization. Consequently, the time-consuming performance is limited by the physical fact that many sorts of SMs require quite time to become stable. Compared to the offline scheme, which requires several seconds for spectra acquisition alone, the time-consuming performance has already been significantly enhanced. Figure 6b illustrates the real-time spectra on the Rx side and the inter-soliton separations after decoding. Calculated separations of the Rx side are nearly consistent with the Tx side, indicating that the system performs real-time signal transmission successfully.

Spectral period doubling of SMs. Benefited from the robust real-time control, we observe a spectral period doubling phenomenon of SMs for the first time in an NPE MLFL, which is very hard to be captured by manual adjustment. This similar phenomenon, which has been observed in single soliton studies, is characterized by two different spectral shapes appearing alternately in two consecutive roundtrips (i.e., spectral period doubling) with periodically varying energies. This intriguing phenomenon can be considered as a bifurcation of the chaotic dynamics, which are typically caused by excessive self-phase modulation (SPM)⁵⁷ in ultrafast fiber lasers or involving cross-phase modulation (XPM)⁵⁸ in vector fiber lasers. The left part of Fig. 7a shows the real-time spectra of 20 consecutive roundtrips in the spectral period doubling state. The spectra of two adjacent roundtrips are different, while the spectra of two nearest but non-adjacent roundtrips resemble to each other, indicating that the switching frequency is equal to the repetition rate. As illustrated in the right part of Fig. 7a, the spectral periodic switching is accompanied by energetic periodic fluctuations and minor periodic changes in the inter-soliton separations of the SMs. The upper two panels in Fig. 7b present the real-time spectra of the two states, respectively, validating the variation of energy distribution at different wavelengths. The energetic variation may be the result of the accumulation of SPM at relatively high energies, which disrupts the equilibrium between the attractive and repulsive forces of the two solitons. The below one in Fig. 7b compares the averaged envelope of two adjacent roundtrips to the spectrum acquired by the OSA. The central part with higher energies is well-aligned but the sides are different from the OSA curve, proving that fast laser dynamics cannot be characterized by the OSA.

Discussion

Thanks to the Lyot filtering effect formed by the weaker nonlinear rotation in the high-concentration fiber and the short cavity, the NPE laser with the high-concentration gain fiber and the short cavity length is more attractive to the generation of SMs⁵⁵. We also manage the intracavity net dispersion to be negative but close to zero by tuning fiber lengths with different dispersion signs, which further facilitates the production of SMs according to our experimental experiences. As a result, we omit SLM incorporating a sophisticated 4-f system enabling powerful tuning on intracavity dispersion, which in turn greatly reduces the complexity of the entire system. On the other hand, the spectral resolution of real-time spectra acquisition is less precise than the OSA, thereby preventing the real-time system from discriminating SMs with excessively dense spectral fringes. Therefore, the current real-time control range over the inter-soliton separation is below 4 ps. Given an ADC with a higher sampling rate or moderately larger dispersion in TS-DFT, the real-time control can reach a greater tuning range and higher precision on the inter-soliton separation control. Moreover, with the improved spectral resolution, peaks and valleys of the spectral fringes can be accurately located thereby extracting the SPR from the single-shot spectra. Thus, the real-time two-dimensional joint control can also be expected.

Further, the communication capacity of the demonstrated transmission is rather small and mainly limited by the slow establishment processes of SMs. Currently, a delay of 0.1 s occupying half of the single-loop time is spent to wait SMs to stabilize after each perturbation in the fine tuning of the optimization

algorithm. Therefore, the overall SMs searching speed will be substantially improved by optimizing of the laser structure stabilizing the SMs more rapidly. Boosting the running clock of the FPGA and algorithmic optimization will further shorten the sending period. According to communication theories, encoding more bits into one symbol is an effective approach to increase the communication capacity. With more precise comprehensive control, more SMs can be used for transmission. Hence, advanced modulation formats based on the inter-soliton separations (e.g., SSM-8, SSM-16, etc.) and orthogonal modulation formats using multiple orthogonal dimensions can be applied to increase the number of bits conveyed in one symbol. The demonstration transmission scheme can support longer distance as long as the real-time spectra do not overlap each other in the time domain.

To summarize, we demonstrate comprehensive control over SMs in an NPE-based MLFL enabled by a dedicated-designed two-step optimization algorithm. With the high-precision offline feedback, we achieved a broad range control over the inter-soliton separation, from 2 ps to 58 ps and high-precision control with an accuracy of 0.05 ps. The other dimension representing the relative intensity between two solitons, SPR, can also be individually controlled. The joint search combining both dimensions is demonstrated via the real-time comprehensive control method. Further, via real-time spectra acquisition based on TS-DFT and real-time algorithms integrated into an FPGA, we achieve the real-time control over inter-soliton separations of SMs. Consequently, real-time transmission between two FPGAs over 30-km SMF is experimentally demonstrated, where the signals are encoded into the separations of SMs via the real-time control. As the spectral period doubling of SMs demonstrated here, the proposed comprehensive control can also contribute to the study of internal dynamics of lasers. We believe this elegant and compact comprehensive control over SMs can find new applications in laser optics and provide inspirations for new possibilities in optical information domains.

Materials and methods

Experimental setup. As shown in Fig. 1a, an erbium-doped MLFL based on NPE is used to study the generation of SMs. The cavity length is 4.8 m, including a 45-cm EDF with a high concentration of 150 dB/m. The dispersion amount of SMF is 17 ps/(nm·km), while the EDF is -48 ps/(nm·km), providing a net dispersion of about -0.0676 ps^2 . The EPC has a microsecond-level response and is driven by four DACs. The four-channel 0–5 V DC signal drives the four-phase retarders with different principle-axis directions inside the EPC. In the offline close-loop control, the spectra are acquired by an OSA (Yokogawa AQ6370D) with the spectral resolution setting at 0.1 nm. In the real-time close-loop control, TS-DFT is performed by the 30-km SMF with a dispersion amount of 510 ps/nm. A 10-GHz PD and a 4-Gsa/s ADC is used for detecting the real-time successive spectra and the spectral resolution of TS-DFT is 0.49 nm.

Theoretical derivations. We consider a SM consisting of two soliton envelopes $E_1(t)$ and $E_2(t)$ with the carrier frequency of ω_0 . The field of this SM can be expressed as shown in Eq. (1).

$$E(t) = \text{Re}\{[E_1(t) + E_2(t)]\exp(i\omega_0 t)\} \quad (1)$$

Then, we assume that the envelope of $E_2(t)$ is similar with $E_1(t)$ but weaker, which can be expressed by an attenuation coefficient α ($0 < \alpha \leq 1$). Thus, $E_2(t)$ can be expressed as Eq. (2), where τ is the inter-soliton separation and $\Delta\varphi$ denotes the relative phase between the two solitons.

$$E_2(t) = \alpha E_1(t + \tau)\exp(i\Delta\varphi) \quad (2)$$

This separation τ causes a stable phase shift of $\exp(i\omega\tau)$ in the frequency domain, which in turn generates coherent fringes with a spectral modulation period of $1/\tau$. The spectral interferogram $|F(\omega)|^2$ is derived as shown in Eq. (3).

$$|F(\omega)|^2 = |E_1(\omega - \omega_0)|^2[\alpha^2 + 2\alpha\cos(\omega\tau - \omega_0\tau + \Delta\varphi) + 1] \quad (3)$$

Drawn from Eq. (3), the spectral interferogram can reach the minimum value of zero only when $\cos(\omega\tau - \omega_0\tau + \Delta\varphi) = -1$ and $\alpha = 1$. It implies the maximum modulation depth of the spectral interferogram is obtained when the two solitons have equal amplitudes, which is the case of the SPR equaling to 0.5. While implementing the TS-DFT, the modulation period of $1/\tau$ in the frequency domain is transferred to the time domain according to the linear mapping given in Eq. (4), where β_2 and L represent the group velocity dispersion and length of the dispersion medium, respectively. Higher-order dispersions are not considered here due to their relatively small dispersion values.

$$\Delta t = 2\pi\beta_2 L/\tau \quad (4)$$

The two-step optimization algorithm. The searching algorithm consists of two major steps, while the first step is to locate the mode-locking states governed by the modified GA. This step focuses on regulating the polarization state in the cavity by optimizing the EPC control voltage. The fitness is the FWHM of the spectral envelope, which should be rather distinguishable between the continuous wave state and mode-locking states since the latter has a significantly broader spectrum.

The second step is a fine-tuning stage where the pump and EPC are driven by tiny perturbations to search the desired SMs on a smaller scale. According to experimental findings, the transformation among different SMs is catalyzed by the variation of energy. Consequently, the voltage signal controlling the pump is designed to mimic a sinusoidal motion with increasing amplitude, gradually extending the range of the fine tuning on the pump power. The voltage is higher than the initial value in the previous half-period and lower in the next half. The voltage ascends more rapidly than it decays, preventing a significant power drop that could cause the laser to unlock. The EPC is driven by four-channel DC

voltages with small random perturbations around 0.2 V. After each adjustment on the pump or the EPC, the current laser status is checked. The modified GA is relaunched for search mode-locking states when the number of consecutive detachments surpasses the preset threshold. Thus, being stuck in the unlocked local area can be avoided. The algorithm exits when the desired SM is found, which means the absolute error between the current fitness and the target fitness is smaller than a preset error threshold.

The fitness in fine tuning is the inter-soliton separation or the SPR, which is derived from the autocorrelation traces obtained by performing fast Fourier transform (FFT) on the spectrum. The positions and intensities of the highest peak and the second-highest peak are extracted. The lateral interval between the two peaks is the separation, and the intensity ratio of the two peaks in the longitudinal direction is the SPR.

Declarations

Author contributions

Chao Luo and Guoqing Pu conceived of the idea, designed the experiments and performed them together. Zhiwei Fang, Yong Wu, Jiajin Wang assisted in the experiment settings. Guoqing Pu and Lilin Yi supervised and directed the conduct of this experiment. All authors discussed the results and contributed to writing the manuscript.

Acknowledgement

This work is supported by the National Natural Science Foundation of China (grant nos. 62227821, 62025503, and 62205199).

Competing interests

The authors declare no competing interests.

References

1. Michael J. Redlich et al. High-pulse-energy multiphoton imaging of neurons and oligodendrocytes in deep murine brain with a fiber laser. *Sci. Rep.* **11**, 7950 (2021).
2. C. Xu & F. W. Wise. Recent advances in fibre lasers for nonlinear microscopy. *Nat. Photonics* **7**, 875–882 (2013).
3. Nathalie Picqué & Theodor W. Hänsch. Frequency comb spectroscopy. *Nat. Photonics* **13**, 146–157 (2019).
4. Xue-Qing Liu et al. Biomimetic sapphire windows enabled by inside-out femtosecond laser deep-scribing. *Photonix* **3**, 1 (2022).
5. Koji Sugioka & Ya Cheng. Ultrafast lasers—reliable tools for advanced materials processing. *Light Sci. Appl.* **3**, e149 (2014).

6. Paolo Ghelfi et al. A fully photonics-based coherent radar system. *Nature* **507**, 341–345 (2014).
7. Yunshan Jiang, Sebastian Karpf & Bahram Jalali. Time-stretch LiDAR as a spectrally scanned time-of-flight ranging camera. *Nat. Photonics* **14**, 14–18 (2020).
8. Nils Nemitz et al. Frequency ratio of Yb and Sr clocks with 5×10^{-17} uncertainty at 150 seconds averaging time. *Nat. Photonics* **10**, 258–261 (2016).
9. B. J. Bloom et al. An optical lattice clock with accuracy and stability at the 10^{-18} level. *Nature* **506**, 71–75 (2014).
10. Scott A. Diddams, Kerry Vahala & Thomas Udem. Optical frequency combs: Coherently uniting the electromagnetic spectrum. *Science* **369**, eaay3676 (2020).
11. Chih-Hao Li et al. A laser frequency comb that enables radial velocity measurements with a precision of 1 cm s^{-1} . *Nature* **452**, 610–612 (2008).
12. B. A. Malomed. Bound solitons in the nonlinear Schrödinger–Ginzburg-Landau equation. *Phys. Rev. A* **44**, 6954-6957 (1991).
13. N. Akhmediev, A. Ankiewicz & J. Soto-Crespo, Multisoliton solutions of the complex Ginzburg-Landau equation. *Phys. Rev. Lett.* **79**, 4047–4051 (1997).
14. D. Tang, W. Man, H. Y. Tam & P. Drummond. Observation of bound states of solitons in a passively mode-locked fiber laser. *Phys. Rev. A* **64**, 033814 (2001).
15. F. M. Mitschke & L. F. Mollenauer. Experimental observation of interaction forces between solitons in optical fibers. *Opt. Lett.* **12**, 355–357 (1987).
16. Wenbin He, Meng Pang, Dung-Han Yeh, Jiapeng Huang & Philip. St. J. Russell. Synthesis and dissociation of soliton molecules in parallel optical-soliton reactors. *Light Sci. Appl.* **10**, 120 (2021)
17. Katarzyna Krupa, K. Nithyanandan, Ugo Andral, Patrice Tchofo-Dinda & Philippe Grelu. Real-time observation of internal motion within ultrafast dissipative optical soliton molecules. *Phys. Rev. Lett.* **118**, 243901 (2017).
18. Junsong Peng et al. Breather Molecular Complexes in a Passively Mode- Locked Fiber Laser. *Laser Photon. Rev.* **15**, 2000132 (2021).
19. A. Hause, H. Hartwig, M. Böhm & F. Mitschke. Binding mechanism of temporal soliton molecules. *Phys. Rev. A* **78**, 063817 (2008).
20. Philippe Grelu & Nail Akhmediev. Dissipative solitons for mode-locked lasers. *Nat. Photonics* **6**, 84–92 (2012).
21. L. Gui et al. Soliton molecules and multisoliton states in ultrafast fibre lasers: Intrinsic complexes in dissipative systems. *Appl. Sci.* **8**, 201 (2018).
22. P. Grelu, F. Belhache, F. Guty & J.-M. Soto-Crespo. Phase-locked soliton pairs in a stretched-pulse fiber laser. *Opt. Lett.* **27**, 966–968 (2002).
23. M. Grapinet & P. Grelu. Vibrating soliton pairs in a mode-locked laser cavity. *Opt. Lett.* **31**, 2115–2117 (2006).

24. Hidetsugu Sakaguchi, Dmitry V. Skryabin & Boris A. Malomed. Stationary and oscillatory bound states of dissipative solitons created by third-order dispersion. *Opt. Lett.* **43**, 2688-2691 (2018)
25. Tianyu Zhu, Zhaokun Wang, D. N. Wang, Fan Yang & Liujiang Li. Observation of controllable tightly and loosely bound solitons with an all-fiber saturable absorber. *Photon. Res.* **7**, 61–68 (2019).
26. Ata Mahjoubfar et al. Time stretch and its applications. *Nat. Photonics* **11**, 341–351 (2017).
27. Yudong Cui et al. Dichromatic “Breather Molecules” in a Mode-Locked Fiber Laser. *Phys. Rev. Lett.* **130**, 153801 (2023).
28. Yi Zhou, Yu-Xuan Ren, Jiawei Shi & Kenneth K. Y. Wong. Breathing Dissipative Soliton Molecule Switching in a Bidirectional Mode-Locked Fiber Laser. *Adv. Photonics Res.* **3**, 2100318 (2022).
29. Junsong Peng, Sonia Boscolo, Zihan Zhao & Heping Zeng. Breathing dissipative solitons in mode-locked fiber lasers. *Sci. Adv.* **5**, eaax1110 (2019).
30. Z. Wang, K. Nithyanandan, A. Coillet, P. Tchofo-Dinda & P. Grelu. Optical soliton molecular complexes in a passively mode-locked fibre laser. *Nat. Commun.* **10**, 830 (2019).
31. G. Herink, F. Kurtz, B. Jalali, D. R. Solli & C. Ropers. Real-time spectral interferometry probes the internal dynamics of femtosecond soliton molecules. *Science* **356**, 50–54 (2017).
32. X. Liu, X. Yao & Y. Cui. Real-time observation of the buildup of soliton molecules. *Phys. Rev. Lett.* **121**, 023905 (2018).
33. W. He et al. Formation of optical supramolecular structures in a fibre laser by tailoring long-range soliton interactions. *Nat. Commun.* **10**, 5756 (2019).
34. Yadong Wang et al. Universal mechanism for the binding of temporal cavity solitons. *Optica* **4**, 855-863 (2017).
35. P. Ryczkowski et al. Real-time full-field characterization of transient dissipative soliton dynamics in a mode-locked laser. *Nat. Photonics* **12**, 221–227 (2018).
36. H. Liang et al. Real-time dynamics of soliton collision in a bound-state soliton fiber laser. *Nanophotonics* **9**, 1921–1929 (2020).
37. Siyun Huang et al. Isomeric dynamics of multi-soliton molecules in passively mode-locked fiber lasers. *APL Photonics* **8**, 036105 (2023).
38. Wang, Z. et al. Simultaneous generation and real-time observation of loosely bound solitons and noise-like pulses in a dispersion-managed fiber laser with net-normal dispersion. *Opt. Express* **28**, 39463-39474 (2020).
39. Youjian Song, Defeng Zou, Omri Gat, Minglie Hu & Philippe Grelu. Chaotic Internal Dynamics of Dissipative Optical Soliton Molecules. *Laser Photon. Rev.*, 2300066 (2023).
40. Defeng Zou, Youjian Song, Omri Gat, Minglie Hu & Philippe Grelu. Synchronization of the internal dynamics of optical soliton molecules. *Optica* **9**, 1307-1313 (2022).
41. Youjian Song, Feng Zhou, Haochen Tian & Minglie Hu. Attosecond timing jitter within a temporal soliton molecule. *Optica* **7**, 1531-1534 (2020).

42. Rohrmann P, Hause A. & Mitschke F. Solitons Beyond Binary: Possibility of Fibre-Optic Transmission of Two Bits per Clock Period. *Sci. Rep.* **2**, 866 (2012).
43. Yi Zhou, Yu-Xuan Ren, Jiawei Shi, Huade Mao & Kenneth K. Y. Wong. Buildup and dissociation dynamics of dissipative optical soliton molecules. *Optica* **7**, 965-972 (2020).
44. Peng, J. & Zeng, H. Build-Up of Dissipative Optical Soliton Molecules via Diverse Soliton Interactions. *Laser Photon. Rev.* **12**, 1800009.1-1800009.7 (2018).
45. Veronika Tsaturian et al. Polarisation Dynamics of Vector Soliton Molecules in Mode Locked Fibre Laser. *Sci. Rep.* **3**, 3154 (2013).
46. Rohrmann P, Hause A. & Mitschke F. Two-soliton and three-soliton molecules in optical fibers. *Phys. Rev. A* **87**, 043834 (2013).
47. S. M. Alamoudi, U. Al Khawaja & B. B. Baizakov. Averaged dynamics of soliton molecules in dispersion-managed optical fibers. *Phys. Rev. A* **89**, 053817 (2014).
48. M. Stratmann, T. Pagel & F. Mitschke. Experimental observation of temporal soliton molecules, *Phys. Rev. Lett.* **95**, 143902 (2005).
49. M. Pang, W. He, X. Jiang & P. St. J. Russell. All-optical bit storage in a fibre laser by optomechanically bound states of solitons. *Nat. Photonics* **10**, 454–458 (2016).
50. Yusong Liu et al. Phase-tailored assembly and encoding of dissipative soliton molecules. *Light Sci. Appl.* **12**, 123 (2023).
51. Shilong Liu, Yudong Cui, Ebrahim Karimi & Boris A. Malomed. On-demand harnessing of photonic soliton molecules. *Optica* **9**, 240-250 (2022).
52. F. Kurtz, C. Ropers & G. Herink. Resonant excitation and all-optical switching of femtosecond soliton molecules. *Nat. Photonics* **14**, 9–13 (2020).
53. Luca Nimmesgern, Cornelius Beckh, Hannes Kempf, Alfred Leitenstorfer & Georg Herink. Soliton molecules in femtosecond fiber lasers: universal binding mechanism and direct electronic control. *Optica* **8**, 1334-1339 (2021).
54. J. Girardot, A. Coillet, M. Nafa, F. Billard, E. Hertz & Ph. Grelu. On-demand generation of soliton molecules through evolutionary algorithm optimization. *Opt. Lett.* **47**, 134-137 (2022).
55. W. C. Chen, Z. C. Luo, W. C. Xu, D. A. Han & H. Cao. Effect of gain media characteristics on the formation of soliton molecules in fiber laser. *Laser Phys.* **21**, 1919–1924 (2011).
56. G. Pu, L. Yi, L. Zhang & W. Hu. Genetic Algorithm-Based Fast Real-Time Automatic Mode-Locked Fiber Laser. *IEEE Photonics Technology Letters* **32**, 7-10 (2020).
57. Wang, Z., Coillet, A., Hamdi, S., Zhang, Z. & Grelu, P. Spectral Pulsations of Dissipative Solitons in Ultrafast Fiber Lasers: Period Doubling and Beyond. *Laser Photon. Rev.* **17**, 2200298 (2023).
58. Cui, Y. et al. XPM-Induced Vector Asymmetrical Soliton with Spectral Period Doubling in Mode-Locked Fiber Laser. *Laser Photon. Rev.* **15**, 2000216 (2021).

Figures

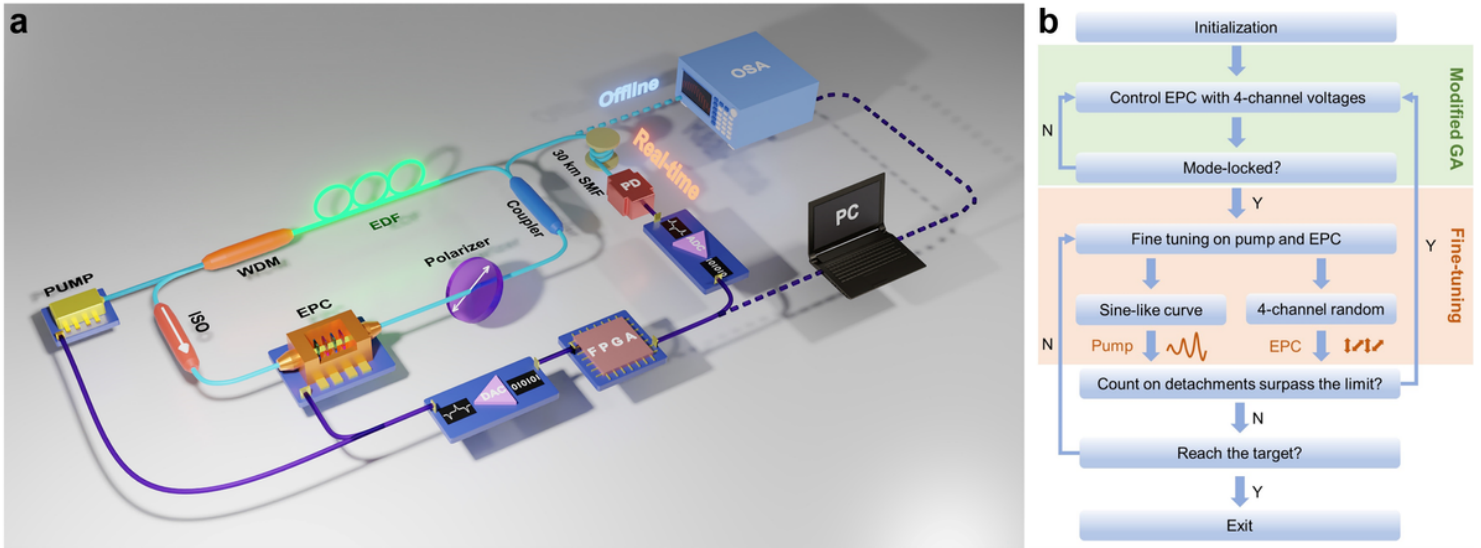


Figure 1

The experimental setup and principles of the optimization algorithm. a, The experimental setup.

Controlling the SMs in the NPE laser can be done in an offline feedback loop and a real-time feedback loop. The spectral information is obtained through the OSA or TS-DFT, where the 30-km SMF is used as the dispersion medium, respectively. Blue lines denote fiber links, and purple lines represent electrical connections. WDM, wavelength division multiplexing; EDF, erbium-doped fiber; Pump, 980nm; ISO, isolator; EPC, electronic polarization controller; PD, photodiode; ADC, analog-to-digital converter; DAC, digital-to-analog converter; FPGA, field-programmable gate array; OSA, optical spectrum analyzer. **b**,

Principles of the optimization algorithm. The modified GA is initially launched to search the mode-locking states. The red area denotes the fine-tuning step, encompassing the identification of SMs and the perturbations over the pump power and the polarization state to search the desire SM.

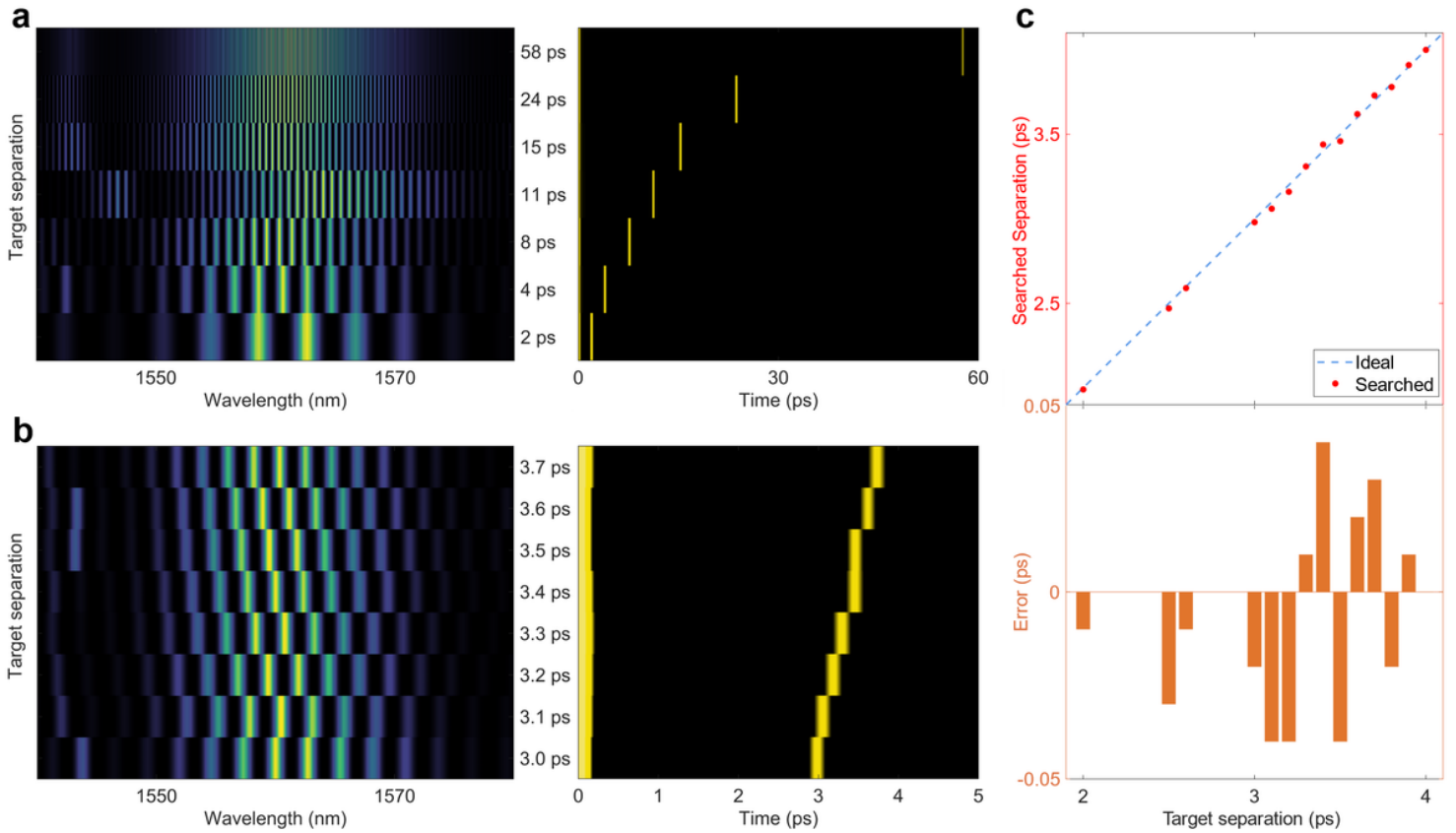


Figure 2

Large-range and high-precision control over inter-soliton separations of SMs. **a**, The spectra of SMs (Left) with inter-soliton separations ranging from 2 to 58 ps, accompanied by the corresponding autocorrelation traces (Right). **b**, The spectra of SMs (Left) with inter-soliton separations ranging from 3.0 to 3.7 ps with the interval of merely 0.1 ps, along with the corresponding autocorrelation traces (Right). **c**, Comparison of target separations and searched separations (Top). The blue dashed line indicates the ideal situation and the red scatters denote actual search data. Errors between target and searched separations (Bottom), demonstrating the high-precision adjustment within 0.05 ps.

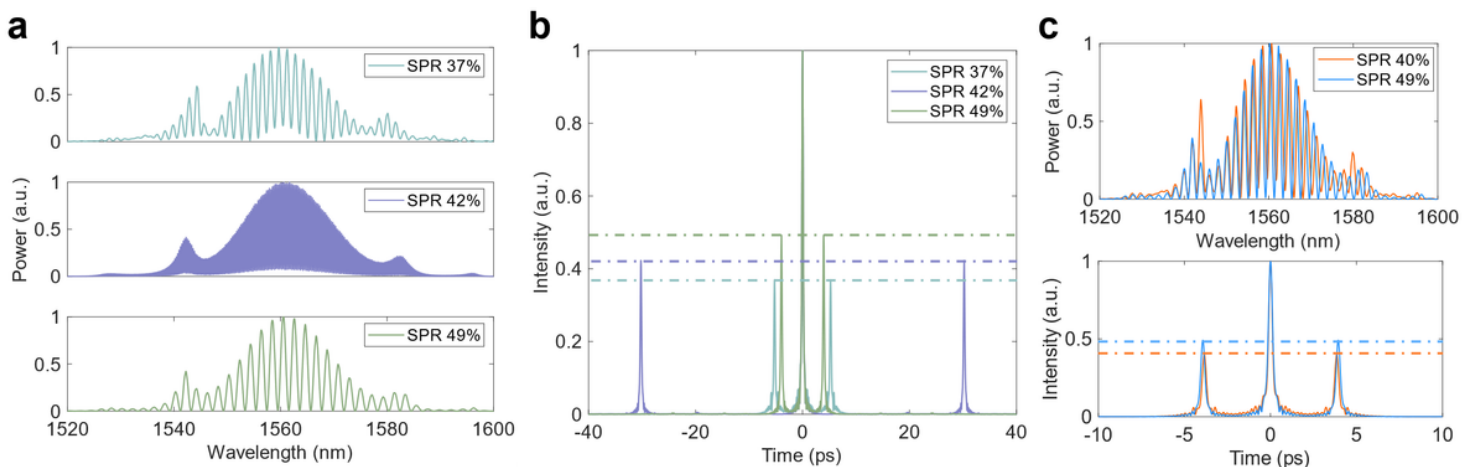


Figure 3

Control over the SPRs of SMs and two-dimensional joint search. **a, b**, The spectra of SMs with 3 different SPRs, and the autocorrelation traces (Right). **c**, Two-dimensional joint search results of searching two SMs with different SPRs but the nearly same inter-soliton separations. The blue curve represents a separation of 3.94 ps and an SPR of 49%, while the orange curve represents a separation of 3.86 ps and an SPR of 40%.

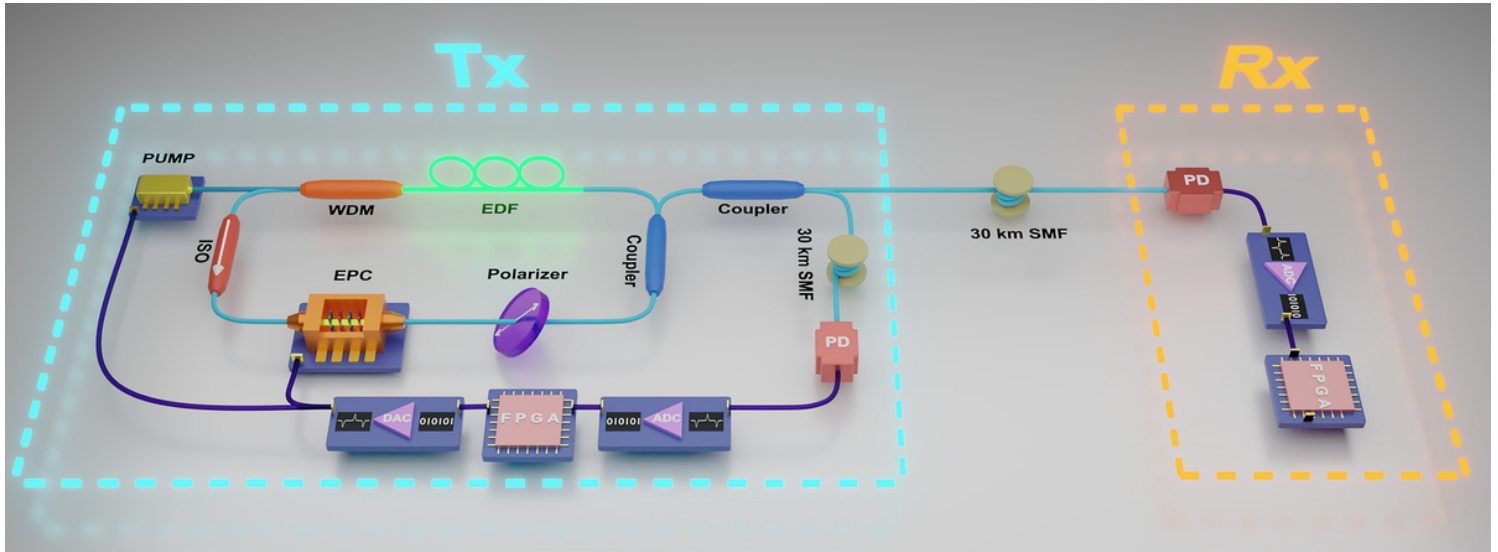


Figure 4

The experimental setup for the soliton separation modulation (SSM)-based real-time transmission. The Tx side includes both the search and recognition sections. The Rx side only includes the recognition section consisting of a PD, an ADC and an FPGA. The 30-km SMF between the Tx and the Rx not only serves as the transmission medium, but also provides necessary dispersion for performing TS-DFT on the sent SMs. Blue lines denote fiber links and purple lines represent electrical connections.

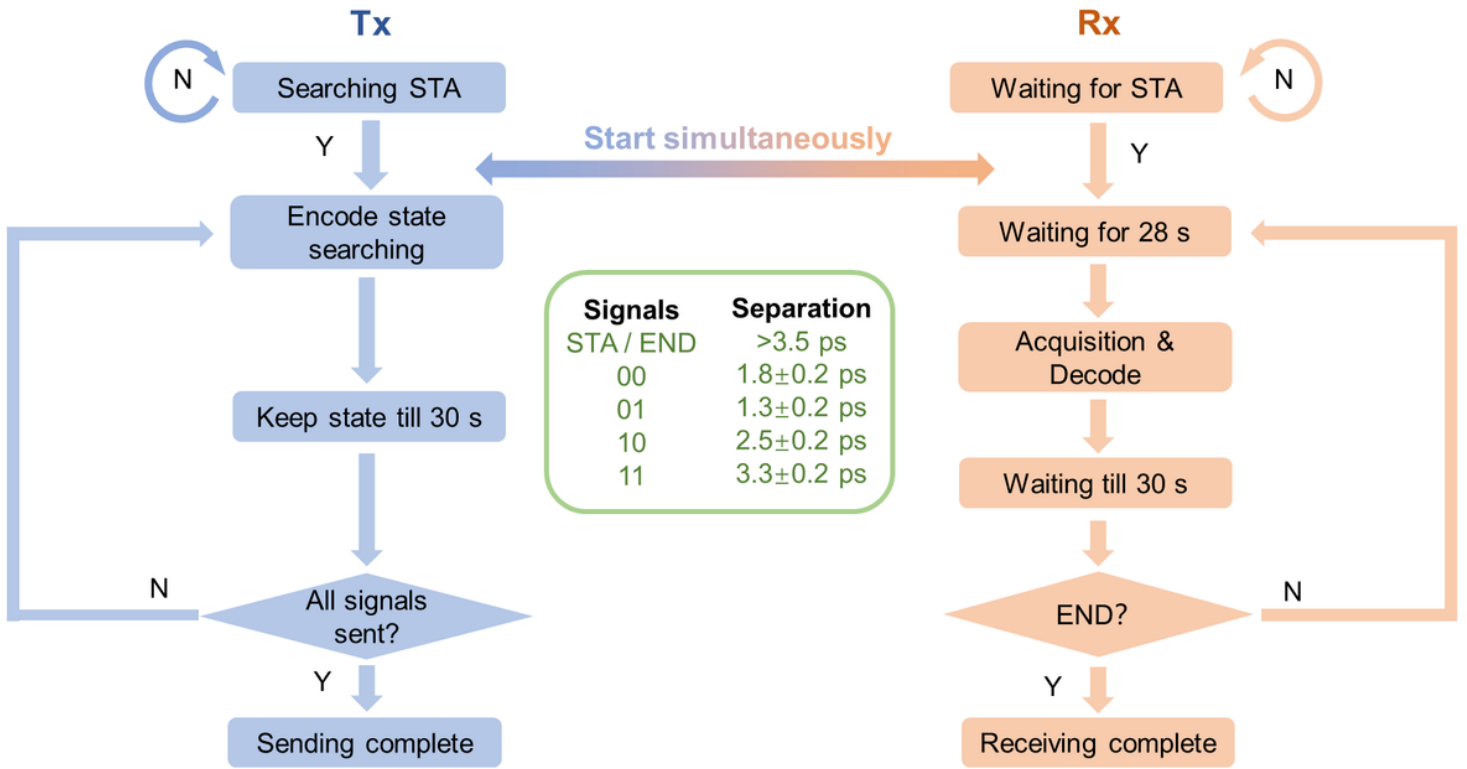


Figure 5

Synchronized communication protocol of the SSM-based real-time transmission. The blue section represents the logic operating on the Tx side, whereas the red section represents the Rx side. The synchronous start of the system depends on the emergence of the start signal (i.e., “STA”). A sending period of 30 s is guaranteed by an interrupt timer, during which the Tx searches the desired SM and maintains the state till the end of the timer, while the Rx completes sampling and recognition. The green box in the middle indicates the correspondence between the encoded signals and the inter-soliton separations.

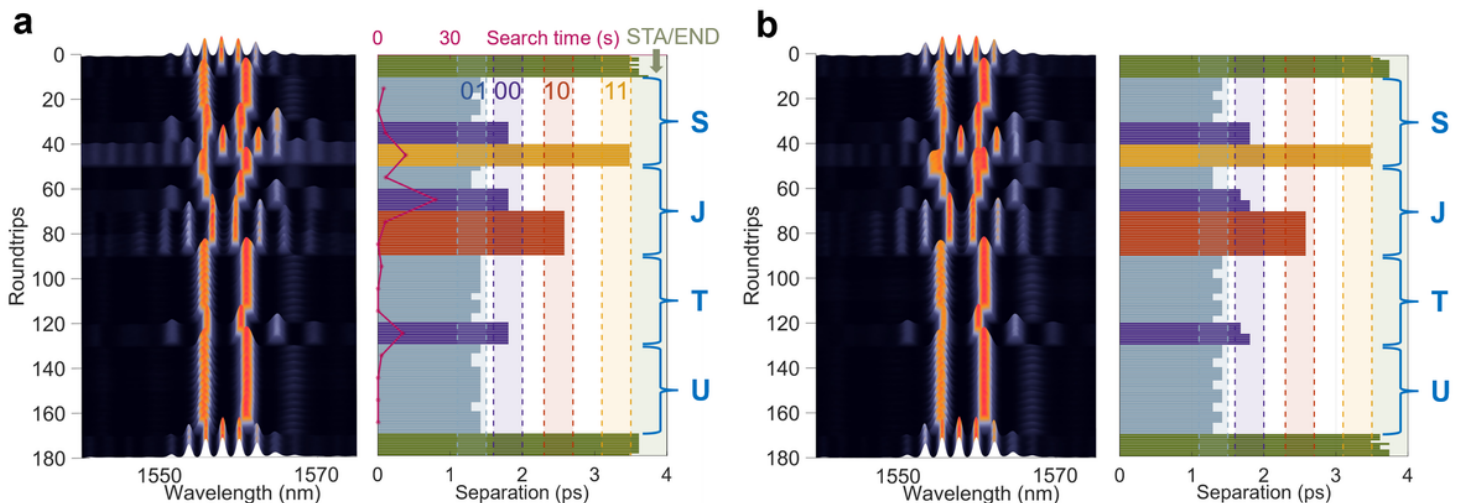


Figure 6

Experiment results of the SSM-based real-time transmission. **a**, 18 encoded signals at the Tx side, including the start and stop signal, with each signal displaying its spectrum for 10 roundtrips (Left). The extracted separations of searched SMs at the Tx side are depicted using different-color histograms, and the shaded areas represent the judgment intervals (Right). Blue represents “01”, purple represents “00”, red represents “10”, yellow represents “11”, and green represents “STA/END”. The 16 valid 2-bit signals together form the “SJTU” string. The pink line indicates the search time for each SM. **b**, 18 signals simultaneously received at the Rx side, including the start and stop signal, with each signal displaying its spectrum for 10 roundtrips (Left). Decoded separations of the received SMs at the Rx side (Right).

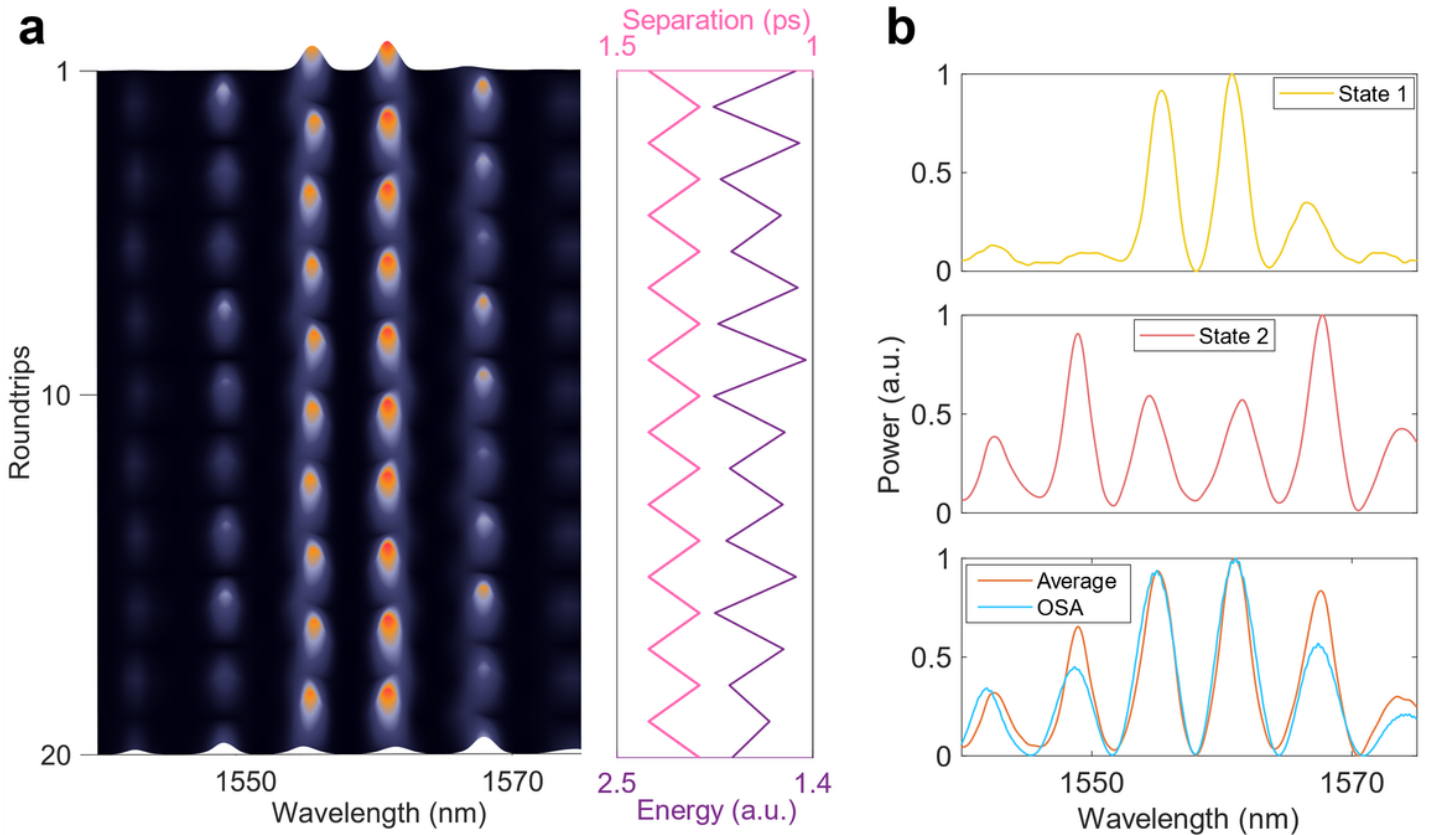


Figure 7

Spectral period doubling of SMs. **a**, The left part indicates the real-time spectral variation over 20 roundtrips. The right part shows the periodic variations in energy and separations. **b**, The upper two panels show the single period real-time spectra of the two alternating states. The bottom one compares the spectrum acquired by the OSA to the average spectrum via superimposing the two alternating states.